



Synthesis and characterization of a xonotlite fibers–silica aerogel composite by ambient pressure drying

Ming Li¹ · Hongyi Jiang¹ · Dong Xu¹

Published online: 26 December 2017
© Springer Science+Business Media, LLC, part of Springer Nature 2017

Abstract

Xonotlite fibers (XFs) reinforced silica aerogel composites were prepared by a sol–gel method under ambient pressure drying. XFs were synthesized through a dynamic hydrothermal route and had a noodle-like structure with length of 5–10 μm and average diameter of 150–200 nm. The microstructure analysis showed that XFs were inlaid in silica aerogel matrix by physical combination which contributed to restrict the volume shrinkage of alcogels and maintain the integrity aerogels during drying process. The physical, nanoporous and thermal properties of the as prepared aerogel composites were investigated and discussed in detail. The new aerogel composites possessed porous nanostructure, which exhibited typical properties of 0.126 g/cm^3 density, 4.132 cm^3/g pore volume, and thermal conductivity of 0.0285 $\text{W}/(\text{m K})$. The results indicated that the introduced XFs didn't significantly alter the porosity, hydrophobicity or thermal conductivity of aerogel matrix. It was also found that the aerogel composites had much more outstanding porosity than that of pure aerogel upon calcinations at 800 $^\circ\text{C}$. This study fabricated XFs–silica aerogel composites and explored a new way for silica aerogels to endure and remain monolithic under ambient pressure drying.

Keywords Xonotlite fibers · Silica aerogel · Ambient pressure drying · Shrinkage · Thermal conductivity

1 Introduction

Silica aerogels have many unique physical properties such as low bulk density, low thermal conductivity and high surface area [1–4]. They are promising candidates for various applications [3], including space exploration [5], oil spills clean-up [6], catalytic supports [7], sound absorption [8], and especially lightweight thermal insulators [9–11]. Silica aerogels have also found potential applications in the field of thermal packaging and building energy conservation. Some researchers have estimated that aerogel-based building insulation has the potential to reduce 30% of energy consumption and 25% of CO_2 emissions [12] as compared to the currently used insulation materials, such as expanded polystyrene, polyurethane foam, and mineral wool insulation. Silica aerogels can be used in the form of monolith, granulates, or powders,

while the monolithic silica aerogels are the most widely used form among the promising potential applications. In most cases, silica aerogels are dried at supercritical conditions of the solvent to maintain the integrity of aerogel structure. Supercritical drying procedure involves complicated process which are both time and cost intensive. For convenient manufacture and widespread application of silica aerogels, it is necessary to overcome the high manufacturing costs of supercritical drying method. At present, ambient pressure drying technique which involves aging and surface modification has evolved as an effective method to remove the entrapped pore solvents from the wet gels while maintaining the unique texture and excellent properties. However, bulk silica aerogels usually crack into pieces under ambient pressure drying [13–15] due to the inherent fragility which results from the nanostructured silica network—the silica aerogel skeleton comprises highly open structure and the matrix consists of cross-linked long chains of loosely bonded amorphous silica nanoparticles. In order to keep the initial monolithic shape of the gel under ambient pressure drying, composite approach is widely applied. Generally, reinforcing the structure with dispersed fibers or fiber mats to prepare fiber/aerogel multiphase composites have been

✉ Ming Li
wut0606@126.com

✉ Hongyi Jiang
jianghy@whut.edu.cn

¹ School of Materials Science and Engineering, Wuhan University of Technology, Wuhan 430070, China

the most common. For the methods of adding fibers, the simplest way to synthesize these type of composites is by introducing short fibers to the solution of the silica precursor before gelation reaction. Yang et al. [16, 17] added inorganic ceramic fibers (3–4 cm long and 4–5 μm in diameter in the amount of 7% of the volume) into silica sol directly to fabricate a fiber-reinforced aerogel composite by supercritical drying method. Yuan et al. [18] fabricated silica aerogel/glass fiber composites by press forming of silica aerogel powders and dispersed glass fibers which were 12 μm in diameter and cut into 3 mm long. Zhang and coworkers [19] applied organic aramid fibers that were more than 10 cm long and 5 to 15 μm in diameter in the amount of 5 wt% as the silica aerogel frame. Ślosarczyk et al. [20, 21] developed carbon microfibers–silica aerogel composites dried both in supercritical and ambient pressure conditions. The reinforcement of carbon microfibers has 700 μm length and 13 μm diameter and was in the amount of 15 wt% of silica aerogel mass. Before being introduced to precursor (tetraethylorthosilicate or tetramethylorthosilicate) solution, the carbon microfibers were pretreated chemically in hot nitric acid. Recently, cellulose nanofibrils or short cellulose fiber have aroused wide concern among researcher. Koebel et al. [22] reported a biopolymer–silica aerogel composite by forming an inter-penetrating silica network inside a silylated nanofibrillated cellulose scaffold. By using methoxytrimethylsilane silica precursor and recycled cellulose fibers that generated from paper waste, Feng et al. [23] developed silica–cellulose aerogels which exhibited better flexibility than that of pure silica aerogels. In the reported literatures, the cellulose/aerogel composites are mostly fabricated by supercritical drying or freeze-drying method. Generally, the organic fibers help to improve the elasticity of the silica matrix, but they lower its resistance to high temperatures, whereas the inorganic fibers (e.g. ceramic or glass fibers) contribute to the improvement of the integrity and thermal resistance of the composite aerogels, but very often increase the density and deteriorate thermal insulation property. Simultaneously, in most studies the inorganic fibers selected for preparation of composites had diameter above several microns that were much greater than the size of nanostructure of silica aerogel network. Consequently, the capillary tension exerted on the interface of the fiber reinforcement and aerogel matrix will be very large during drying process, resulting in a weak interaction between the two different phases. It's therefore necessary to find some other fibers with thinner diameter and less density, aiming at that the fiber-reinforced composites don't sacrifice the advantages of low density while have a strong interaction between the fibers and aerogel matrix. Xonotlite ($6\text{CaO}\cdot 6\text{SiO}_2\cdot \text{H}_2\text{O}$) fiber is a kind of fibrous crystal, which has attracted much attention in thermal insulation and flame retardant fields due to its characteristics of ultra-light property and thermal stability. Moreover, with large

aspect ratio, xonotlite fiber (XF) is also potential candidate as reinforcement component in composite materials, e.g. silica aerogel composites.

In this research, we fabricated XFs reinforced silica aerogel composites via a sol–gel method and ambient pressure drying. Tetraethoxysilane (TEOS) and alkaline silica sol were used as a mixed precursor for the preparation of silica aerogels. The alkaline silica sol is an aqueous colloidal solution of mono-dispersed SiO_2 nanoparticles and very small amounts of sodium cations, thus playing a double role of increasing pH value for gelation reaction and as co-precursor. XFs were synthesized from silicon and calcium species by dynamic hydrothermal method. The XFs products of hydrothermal reaction were filtrated and directly added into the precursor solution at a certain concentration. By a process of constant stirring and ultrasound bath, XFs were uniformly distributed in the liquid phase and interspersed among the three-dimensional silica network with the formation of alcogel. We found that using XFs to generate silica aerogel composites was a frequent and effective method to fabricate monolithic and crack-free aerogel materials under ambient pressure drying, while caused little increase of thermal conductivity or loss of porosity compared to that of the pure silica aerogels.

2 Experimental

2.1 Raw materials

TEOS, ethanol, alkaline silica sol (pH value 9.9; solid content: 26.8%; particle size 8–10 nm), trimethylchlorosilane (TMCS), n-Hexane, *N,N*-dimethylformamide (DMF), HCl solution (0.5 M), deionized water (H_2O), calcium chloride (CaCl_2), silicic acid (H_2SiO_3), potassium hydroxide (KOH), all the chemicals are reagent grade and used as purchased.

2.2 Preparation of XFs

CaCl_2 and H_2SiO_3 solids were respectively dissolved in a KOH solution (2 mol/l) to prepare $\text{Ca}(\text{OH})_2$ suspension and K_2SiO_3 solution while $\text{CaCl}_2\text{:H}_2\text{SiO}_3\text{:KOH}$ molar ratio was fixed at 1:1:2. The mixture of $\text{Ca}(\text{OH})_2$ suspension, K_2SiO_3 solution and deionized water was poured into an autoclave with a stirrer. XFs were synthesized by treating the mixture under the following dynamic hydrothermal condition: solid–liquid ratio of 1:12 g/ml, a heating rate of 5 $^\circ\text{C}/\text{min}$ from room temperature to 220 $^\circ\text{C}$, reaction time of 16 h, stirring rate of 230 rpm. After reaction for given procedure, the mixture was cooled down naturally. At the end, the product was separated by filtration, washed three times with distilled water, and a slurry of 14.3 wt% purified XFs was obtained for use.

2.3 Fabrication of XFs/aerogels

All XFs–silica wet gels were prepared based on sol–gel process by mixing two solutions which were denoted as A and B. Solution A contained a mixture of TEOS, ethanol, DMF and deionized water. TEOS was hydrolyzed using 0.5 M HCl for 24 h at 25 °C while TEOS:ethanol:DMF:water:HCl molar ratio was fixed at 1:9:0.5:2:6.5 × 10⁻⁴. Solution B contained a mixture of alkaline silica sol/ethanol/deionized water with volume ratio of 5:2:3. The alkaline silica sol/TEOS molar ratio was maintained as 0.35. Various percentages of mass content (0, 2.1, 4.2, 8.4, and 16.8%) for XFs added with respect to silica in TEOS and alkaline silica sol were used to control the amount of XFs incorporated into the XFs/aerogels. In a typical procedure, the slurry of purified XFs was added into solution A after the hydrolysis of TEOS and vigorously stirred for 10 min. Then, solution B was poured into solution A under constant stirring for 5 min and sonicated for 3 min. Subsequently, the mixture was poured into molds for gelation in the atmosphere and the XFs/alcogels usually formed in 30 min. XFs/alcogels were aged for 12 h at 35 °C to further accelerate the condensation reaction, and subsequently placed in a 4:1 mixture of ethanol and water for 24 h to strengthen the network structure. The ethanol in the wet silica gels was exchanged with n-Hexane. Surface modification was carried out by immersing the gels in 10% TMCS/n-Hexane solution for 24 h at 25 °C. The gels were then washed with fresh n-Hexane to eliminate the reaction products and unreacted TMCS. Finally, the XFs/aerogels were obtained by drying gels at 60 °C for 12 h and 90 °C for 2 h. Figure 1 highlights the steps of synthesis process.

2.4 Methods of characterization

The phase compositions of the obtained XFs were determined using X-ray diffraction (XRD, D/MAX-RB). The

morphology of the XFs and XFs/aerogels was observed by field emission scanning electron microscope (FESEM, Zeiss Ultra Plus).

The bulk density (ρ) was calculated from mass to volume ratio. The volume was calculated by drainage method while the mass was measured with analytical balance. The percentage of volume shrinkage (V%) was determined from the change in the volume of the alcogel to the aerogel, using the formula: $V\% = (1 - V_a/V_g) \times 100$, where V_a and V_g are the volumes of the aerogel and alcogel respectively.

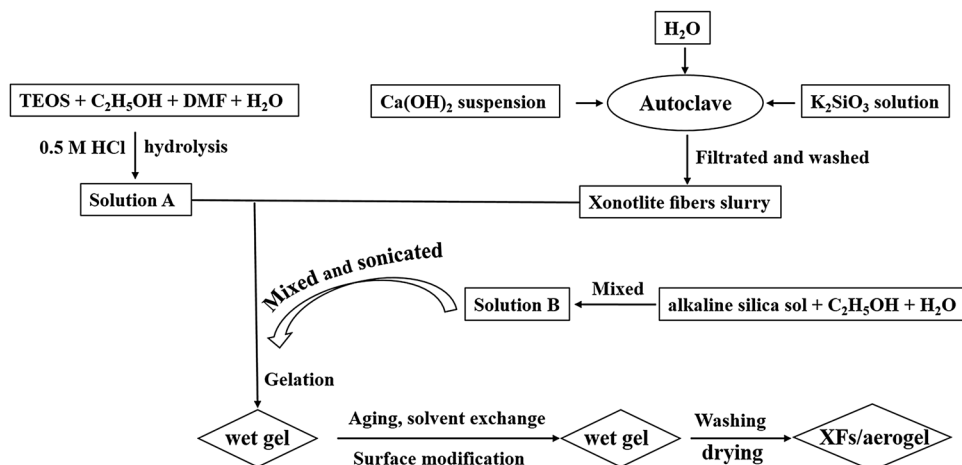
The pore structure was analyzed by N₂ adsorption–desorption isotherms at 77 K of the degassed samples (150 °C for 3 h). Pore volume (V_{BJH}) and pore size distribution were analyzed by BJH method [24] (V_{BJH} includes those measured from the opened pores ranging from 1.7 to 300 nm).

The molecular structure of XFs/aerogels was investigated by a Fourier transform infrared spectroscope (FTIR, Nicolet 6700). Hydrophobicity of the composites was analyzed by measuring the contact angle of the water droplet with the sample surface.

The thermal conductivity of XFs/aerogels was measured with a thermal constants analyzer (Hot-Disk 2500) at 25 °C. The thermal stability analysis was tested using TG-DTA (STA 2500 Regulus) with a heating rate of 10 °C/min from room temperature to 900 °C in air.

To compare the pore structures of pure aerogel and XFs/aerogel at high temperature, the pure aerogel and XFs/aerogel (with XFs content of 8.4%) were calcined at 800 °C in an electrically heated muffle furnace in air for 30 min with a heating rate of 5 °C/min.

Fig. 1 Schematic illustrating the fabrication of XFs/aerogels



3 Results and discussion

3.1 XRD and morphology of XFs

The crystal structures and then the morphology of as-prepared XFs were investigated by the XRD and SEM. In Fig. 2a, the XRD peaks obtained for XFs are perfectly indexed to the characteristic peaks of the monoclinic xonotlite (JCPDS No.: 00-023-0125). The sharp peaks of XRD pattern indicated high crystalline degree of XFs. To define the density of XFs, we dried the slurry of purified XFs at 80 °C in an oven. Then, the fibers were ground and sieved through 200 and 250 mesh sieves. The obtained XFs has tap density of 0.428 g/cm³ and water contact angel of 15.6°. Figure 2b shows the size and the surface morphologies of XFs. The XFs had a noodle-like structure with length of 5–10 μm and average diameter of 150–200 nm, indicating an aspect ratio of approximately 30–50. The randomly collected fibers were free of surface defects and displayed a relatively uniform diameter distribution. The one-by-one flexible fibers with large aspect ratio offered XFs an opportunity for a reinforcement in composites, while the secondary particles of silica aerogel can easily attach on the cylindrical side of XFs.

3.2 Morphology and structure of XFs/aerogel

Figure 3a shows the digital photograph of rod-like XFs/aerogels with different XFs content. XFs/aerogels monolith are intact, opacified and crack-free while the pure silica aerogel is semitransparent and the surface tends to crack. Figure 3b, c shows the 3D porous structure and continuous network of aerogel matrix in XFs/aerogel. As is shown in Fig. 3c, the aerogel matrix is multi porous nanomaterial

with concatenate network structure with dense aggregates of silica spheres. The morphology of fracture surface (Fig. 3d) shows a clear fiber pull-out, which illustrates that the XFs are inset and multidirectional in the aerogel matrix acting as reinforcements. Meanwhile, on the surface of XFs as illustrated in Fig. 3e, silica particles can be detected. From the micrographs, it is observed that the XFs are clearly masked by the aerogel matrix. For the XFs/aerogels composites, nicely embedded XFs in aerogel matrix are presented and the XFs are homogenously wrapped with the aerogel phase to form a “fiber-aerogel-fiber” pattern. The adhesion effect contributes to strengthen the solid skeleton of alcogels to withstand capillary forces during drying process. Therefore, the fiber–matrix is able to keep integrated rather than cracks into some fragments under ambient pressure drying.

3.3 Physical properties and pore structure of XFs/aerogels

The physical properties of all samples are displayed in Table 1. The density of XFs/aerogels ranges from 0.126 to 0.145 g/cm³ as the XFs content varies from 0 to 16.8 wt%. Obviously, the volume shrinkage of samples were significantly affected by the XFs content, namely the volume shrinkage remarkably decreases from 25.1 to 16.2% with an increase of XFs content. Generally, the volume shrinkage during the fabrication process of silica aerogels consists of two parts, i.e., the shrinkage in aging process and the shrinkage in drying process. During ambient pressure drying, the wet gel is contracting due to capillary force and consequently causes the major shrinkage. For the XFs/aerogels composites, XFs were multidirectional and uniform in aerogel matrix and acted as supporting skeleton, which made the wet gel skeleton stronger to withstand the shrinkage during ambient pressure drying. Therefore, the introduced XFs

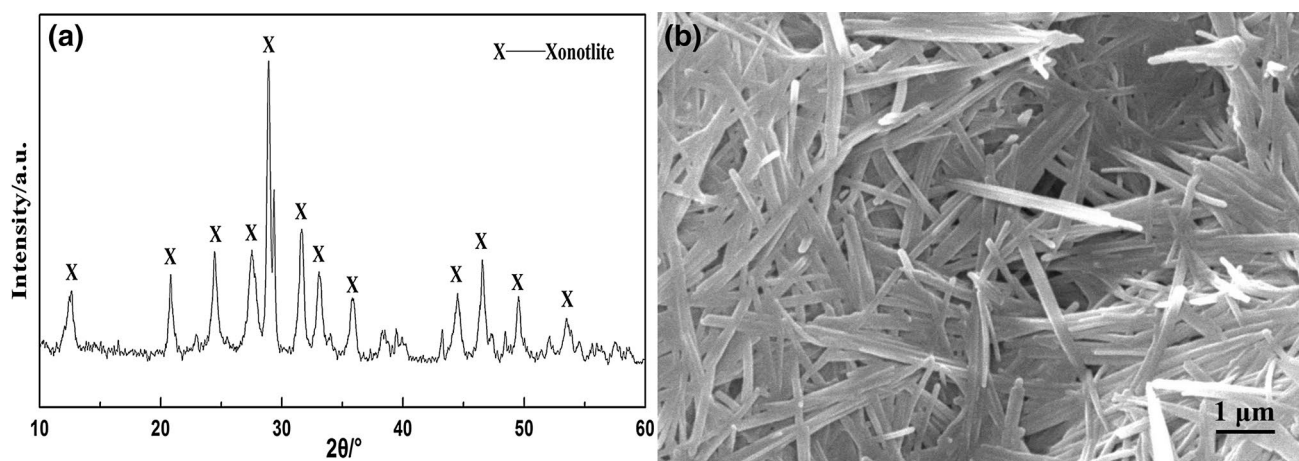


Fig. 2 XRD pattern (a) and SEM image (b) of XFs fibers

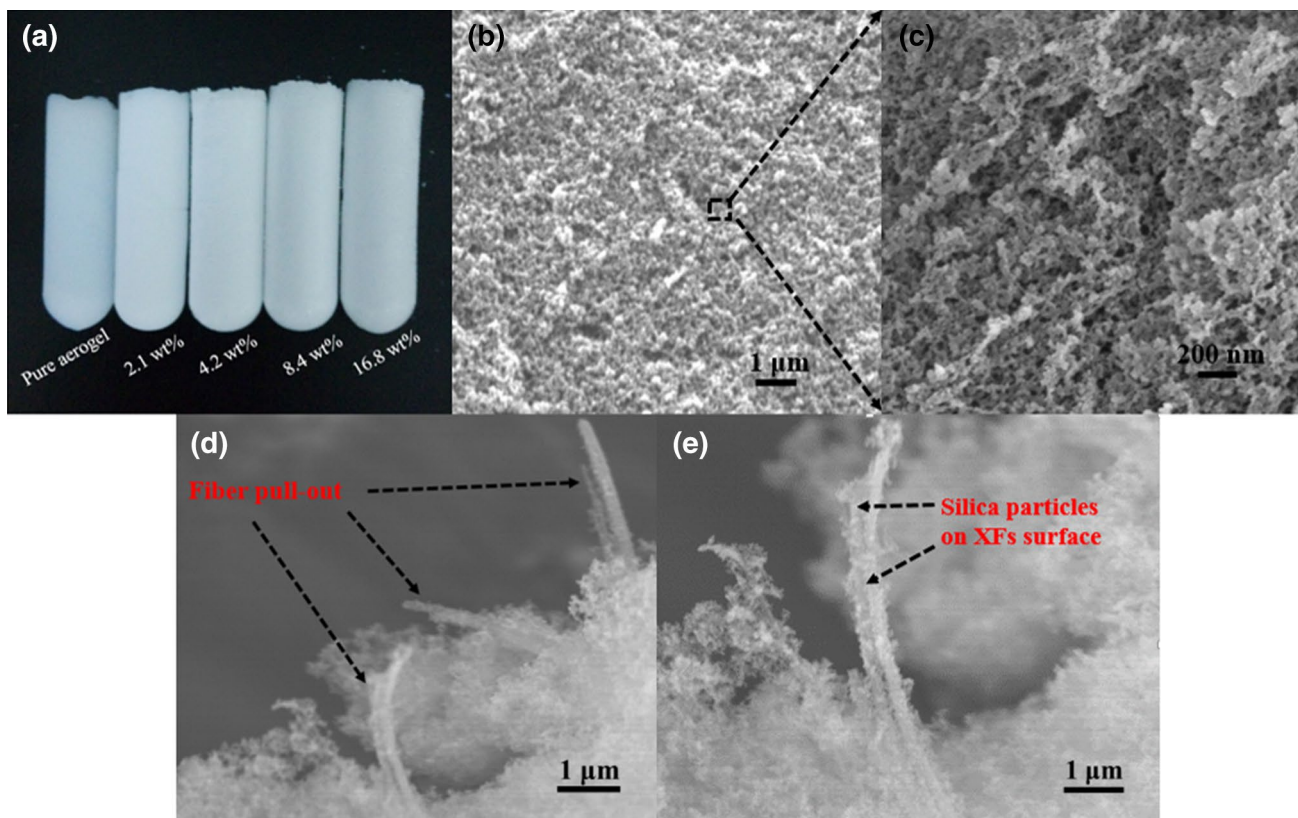


Fig. 3 Morphology and structure of XF/aerogel: **a** photograph of rod-like XF/aerogels; **b, c** nanoporous network of aerogel matrix in XF/aerogel; **d** the fracture surface XF/aerogel; **e** silica particles on the surface of XFs

Table 1 Physical properties of XF/aerogels with various XF content

XF content (wt%)	Volume shrinkage ± 1.5 (%)	Density ± 0.007 (g/cm ³)	BET surface area ± 5.0 (m ² /g)	BJH pore volume ± 0.1 (cm ³ /g)	Average pore size ± 0.2 (nm)
0	25.1	0.138	710.2	3.525	11.9
2.1	24.8	0.141	705.3	3.590	12.1
4.2	24.3	0.132	701.6	3.721	12.8
8.4	20.3	0.126	656.3	4.132	13.9
16.8	16.2	0.145	632.8	3.826	13.6

resulted to a loose silica skeleton and a low density of XF/aerogel at first. On the other hand, since the skeleton density of XF is much bigger than that of the aerogel matrix, a larger amount of XF unexpectedly gave rise to an increase of bulk density of XF/aerogels composites.

The pore structure of XF/aerogels was determined by nitrogen adsorption–desorption measurements. Figure 4 plotted the N₂ adsorption–desorption isotherms and pore size distributions. It is noticeable all of the samples (0, 4.2, and 8.4%) exhibit a type IV isotherm with a small H3-type hysteresis loop (Fig. 4a) which are the characteristic features of the mesopores and slit-like pore geometry according to IUPAC classification [25–27]. Both native aerogel and

XF/aerogels have similar pore size distributions which were multimodal with a strong peak at approximately 16 nm, as is presented in Fig. 4b. This implies that the aerogel samples consist of interpenetrating mesopores, with the most probable pore size of 16 nm. Consequently, we can conclude that the XF/aerogels are mesoporous materials while the introduction of XF does not change the porous structure of the aerogel matrix. The results were in agreement with the previous SEM images. Simultaneously, the data in Table 1 regarding XF/aerogels showed different value of pore volume or surface area. With XF content from 0 to 8.4%, there was a gradual increase in pore volume. As was analyzed previously, the XF prevented the wet gels from shrinking and

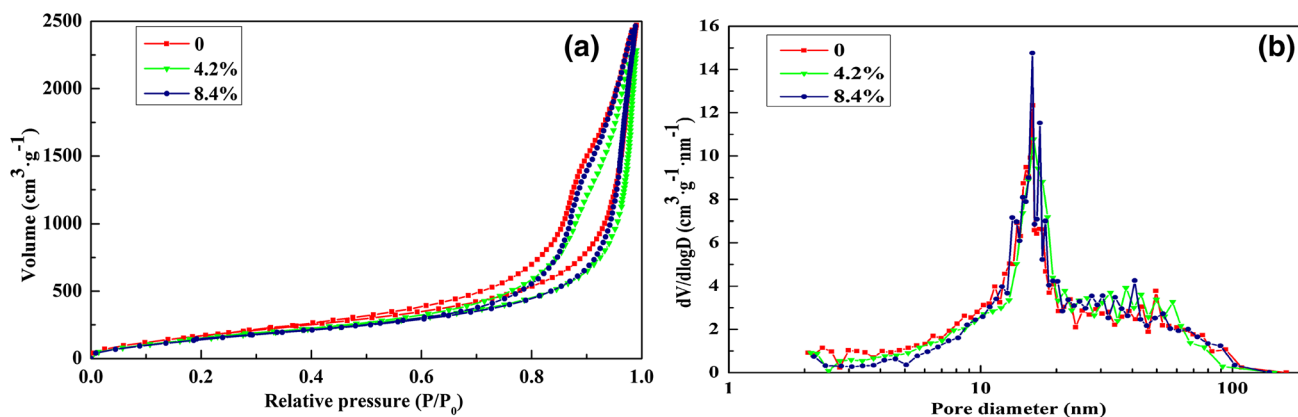


Fig. 4 N_2 adsorption–desorption isotherms (a) and pore size distributions (b) of XF/aerogels with different XF content

subsequently avoided a loss of pores or a decrease of pore size during drying process. Therefore, the XF/aerogels with a proper XF content (8.4%) achieved larger pore volume compared to the native aerogel. With the further increase of XF content to 16.8%, the pore volume of XF/aerogels didn't increase anymore. This is mainly due to the fact that the silica aerogel matrix are partially replaced by XFs, and too much XFs caused an evident decrease of aerogel matrix. Consequently, the XF/aerogels with fibers content to 16.8% exhibit lower pore volume and lower BET surface at the same time.

3.4 Chemical structure and hydrophobicity of XF/aerogels

The FTIR spectra obtained with the pure aerogel and XF/aerogel are presented in Fig. 5a. Typical IR peaks observed in Fig. 5a corresponded to Si–O–Si asymmetric, symmetric and rocking bending vibrations were seen at 1094, 800 and 476 cm^{-1} respectively, for silica materials [28]. The intense peaks appeared mainly around at 2964, 1256 and 847 cm^{-1} belonged to Si–CH₃ while a broad adsorption band existed in the region 3470–3370 cm^{-1} was overlapped with the stretching vibrations of Si–OH and H–OH. The appearance of peak near 1639 cm^{-1} was caused by flexural vibration of H–OH, while a tiny peak near 951 cm^{-1} by rocking bending vibration of Si–OH [29]. After surface modification by TMCS/*n*-Hexane solution, the –OH groups of wet gels were mostly

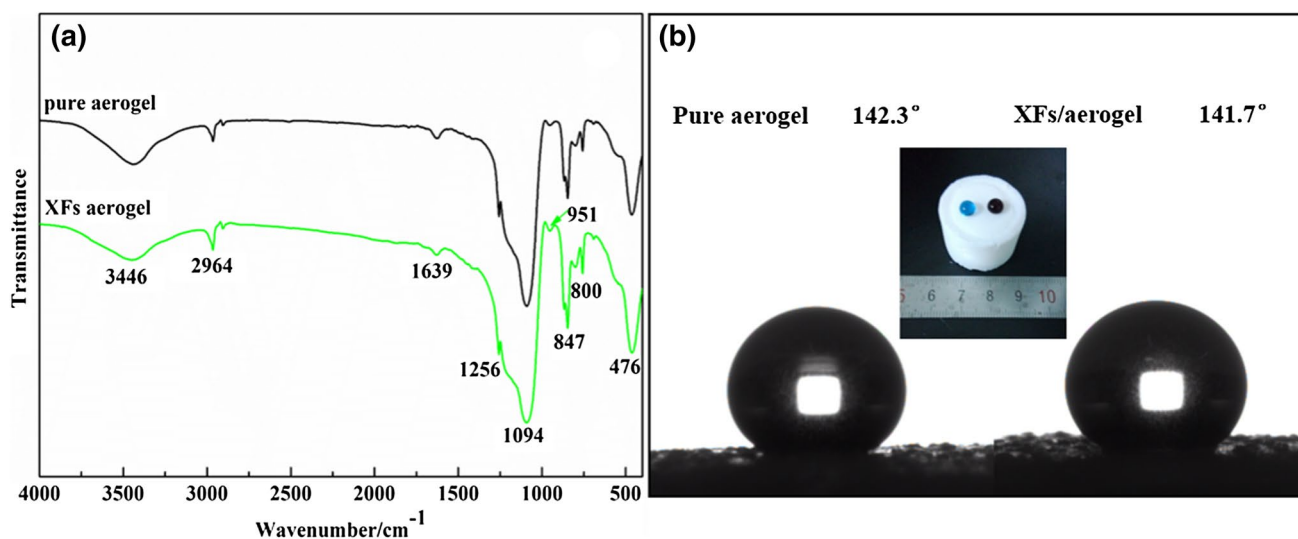


Fig. 5 The hydrophobicity of XF/aerogel: **a** FTIR spectra of pure aerogel and XF/aerogel; **b** water contact angles of pure aerogel and XF/aerogel; inset in **b** is an image of the water droplets formed on the XF/aerogel

substituted by $-\text{CH}_3$ groups and subsequently hydrophobic XFs/aerogels were obtained. The FTIR analysis results are consistent with the water contact angles data. As is shown in Fig. 5b, the water droplets maintained spheroid shape with contact angle of 142.3° for pure aerogel and 141.7° for XFs/aerogel, confirming that the XFs/aerogels do not appear to an obvious decrease of hydrophobicity with the adding of XFs. It is noted that the FTIR spectrum of XF/aerogel in Fig. 5a shows no evidence of the XFs. This is due to the fact that XFs are clearly masked by the aerogel matrix and XFs are not detected by FTIR spectroscopy in most cases. In the meantime, the IR peaks of pure aerogel and XFs/aerogel were nearly identical except peak intensities, which indicated the physical interaction between the two different phases of XFs and silica aerogels.

3.5 Thermal conductivity and thermal stability of XFs/aerogels

Figure 6 shows the thermal conductivities of the pure aerogel and the XFs/aerogels. It can be seen that the thermal conductivity of the prepared silica aerogel samples had a tiny variation from 0.0331 to 0.0285 $\text{W}/(\text{m K})$ with XFs content increasing from 0 to 8.4%. And then, the XFs/aerogels showed a clear tendency of increasing thermal conductivity with the further increase of XFs content. Generally, the thermal energy passing through an insulating material occurs by three mechanisms, i.e. solid conductivity, gaseous conductivity and radiative transmission. The effective thermal conductivity of an insulating material is determined by the sum of these three components. Silica aerogel has a high porosity (usually above 90%) and consists of a quite small fraction of solid silica. The solid skeleton comprises interconnected spherical nano-particles linked in a 3D network. Such a structure has numerous nanopores which can suppress the mean free path of gas and lead to weak convective heat transfer, namely low gaseous thermal conductivity.

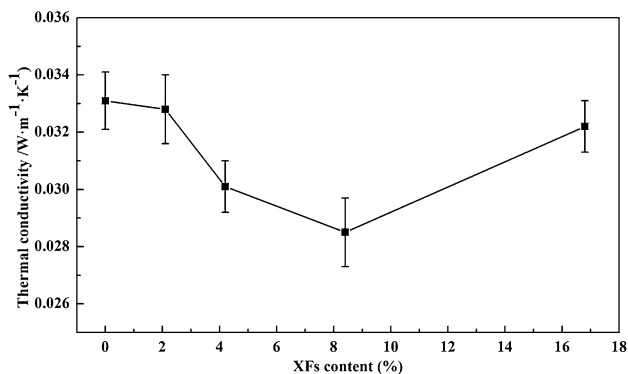


Fig. 6 Thermal conductivity of XFs/aerogels with different XFs content

Meanwhile, the heat conduction from radiative transmission has negligible effect under ambient conditions. Therefore, the major mode of thermal transport through silica aerogels is solid thermal conductivity that has great effect on the aerogel thermal insulation [11, 30]. In the case of XFs/aerogels, solid thermal conductivity occurs through both silica solid backbone and XFs. The XFs produced new heat transfer passageways when they were inlaid in the aerogel nanoporous network, and then more heat transferred through the new passageways instead of the aerogel matrix, owing to the higher solid conductivity of the XFs than that of the pure silica aerogel. It should also be noted that, the XFs strengthened the solid skeleton of wet gels to withstand capillary forces and prevented the volume shrinkage during drying process, as was analyzed previously. Compared to the denser silica skeleton of pure aerogels, a loose silica skeleton of XFs/aerogels undoubtedly rendered the heat transfer slower and resulted in a less thermal conductivity. That's to say, the effect of XFs amount on thermal conductivity increment was partly offset, attributed to the reduction of volume shrinkage.

A thermal gravimetric analysis up to 900°C in an air atmosphere was performed additionally to investigate the thermal stability of XFs/aerogel. As is depicted in Fig. 7, the obtained curves conveyed the impression that there is no obvious difference between pure aerogel (Fig. 7a) and XFs/aerogel (Fig. 7b) in terms of physical or chemical reactions during the heating process. There is a minor mass change for both pure silica aerogel and XFs/aerogel up to the temperature of 200°C , which is caused by the evaporation of a small quantity of water or organic solvent. On the surface of silicon, there exists abundant $-\text{CH}_3$ groups produced from surface modification. When the temperature is around 415°C , the increase in weight loss turns to be rapid due to the oxidation of the $-\text{CH}_3$ groups along with a sharp exothermic peak in the DTA curve. The oxidation of $-\text{CH}_3$ groups result in the main weight loss of aerogels during the heating process, which are about 8.7% for pure aerogel and 8.2% for XFs/aerogel, respectively. From the above analysis, it's clear that the thermal stability of XFs/aerogels is mainly depended on the silica aerogels matrix. Indeed, the xonotlite is a kind of refractory material which can endure more than 1000°C high temperature and we found that the XFs could help to prevent the pore structure from being completely destroyed at a high temperature. For further studies, the pure aerogel and XFs/aerogel (with XFs content of 8.4%) were calcined at 800°C in an electrically heated muffle furnace in air for 30 min. The heating rate was $5^\circ\text{C}/\text{min}$ from room temperature to final temperature. Figure 8 illustrated a comparison between pure silica aerogel and XFs/aerogel about pores parameters before and after the calcination procedure. After 800°C calcination, the specific surface area of both samples was remarkably reduced, as well as the pore volume, indicating a less

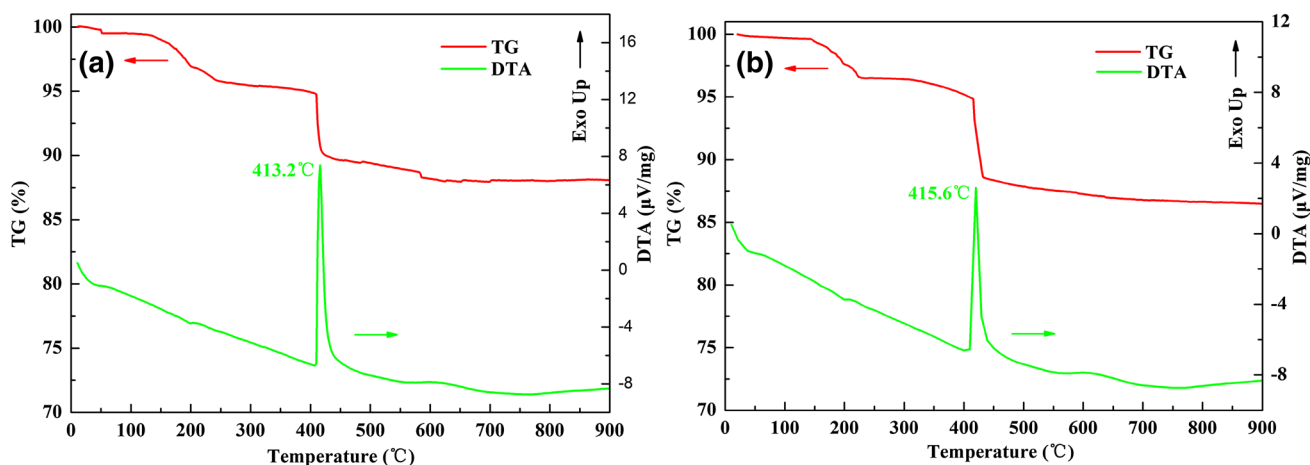


Fig. 7 TG–DTA graphs for pure aerogel (a) and XFs/aerogel (b)

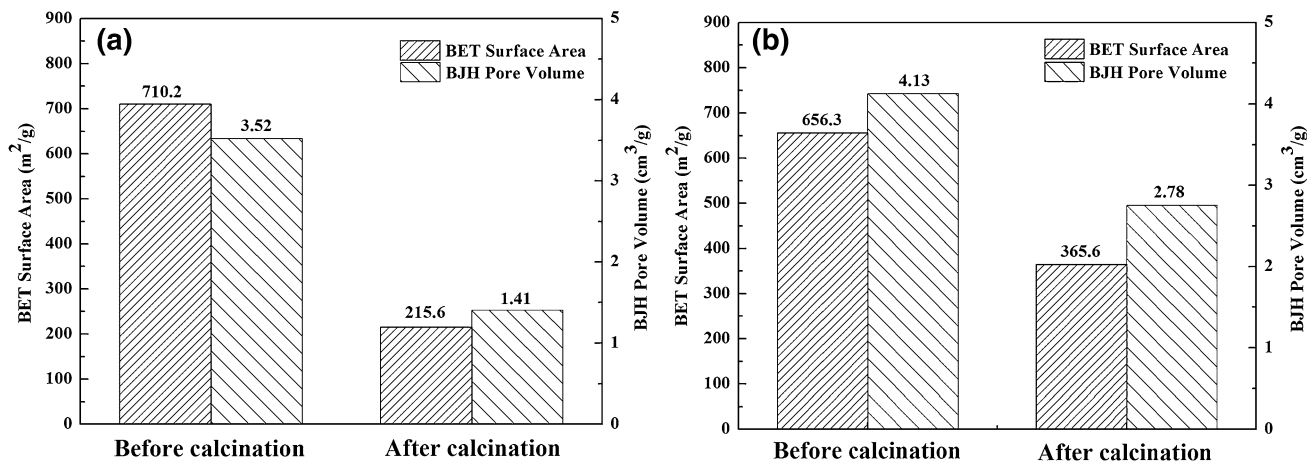


Fig. 8 A comparison between pure silica aerogel (a) and XFs/aerogel (b) about pores parameters before and after the calcination procedure

porous structure. The specific surface area and pore volume for pure aerogel were 215.6 m²/g and 1.41 cm³/g, i.e. a decrease of almost 69.6 and 59.9%, respectively. On the other hand, it is encouraging that the XFs/aerogel keeps a higher specific surface area and pore volume which were 365.6 m²/g and 2.78 cm³/g with a decrease of almost 44.3 and 32.7%, respectively. Clearly, XFs/aerogel had much more outstanding porosity than that of pure aerogel upon calcinations at 800 °C. This phenomenon could be associated with the interaction between XFs and aerogel, and thus the skeleton of XFs/aerogels could be able to avoid full densification upon thermal treatment. Moreover, the doping XFs might obstruct the primary particles of silica aerogel to grow into larger ones during calcination, which also contributed to the maintenance of specific surface area and pore volume. The influence mechanism of the XFs on the porosity of XFs/aerogels at a high temperature

should be explained by a detailed analysis which are now under further investigation.

4 Conclusions

XFes with high aspect ratio were synthesized through a dynamic hydrothermal route and then XFs reinforced silica aerogel composites were prepared successfully via ambient pressure drying. The XFs/aerogels exhibited a favorable interfacial adhesion with XFs inlaying in the aerogel matrix and porous structure of aerogels covering on the surface of XFs, which resulted in composites with unique interpenetrating network that could finally decrease the volume shrinkage of alcogels and retain aerogels integrity during drying process. As the XFs content increased, the bulk density of XFs/aerogels ranged from 0.126 to 0.145 g/

cm³ as well as the volume shrinkage decreased from 25.1 to 16.2%. The FTIR analysis demonstrated the existence of abundant –CH₃ groups on the surface of XFs/aerogels which possessed high hydrophobicity with water contact angle of nearly 142°. Moreover, with a proper XFs content, the XFs/aerogels achieved a lower thermal conductivity of 0.0285 W/(m K) and higher porosity upon calcinations for 30 min at 800 °C than that of pure aerogel.

References

- L.W. Hrubesh, *J. Non-Cryst. Solids* **225**, 335 (1998)
- A.A. Pisal, A.V. Rao, *J. Porous Mater* **24**, 685 (2017)
- M.A. Aegerter, N. Leventis, M.M. Koebel, *Aerogels Handbook* (Springer, New York, 2011), pp. 29–38
- A. Soleimani Dorcheh, M.H. Abbasi, *J. Mater. Process. Technol.* **199**, 10 (2008)
- S.M. Jones, *J. Sol Gel Sci. Technol.* **40**, 351 (2006)
- Mohamed H. Sorour, Heba A. Hani, Ghada A. Al-Bazedi, A.M. EL-Rafei, *J. Porous Mater.* **23**, 1401 (2016)
- M. Domínguez, E. Taboada, E. Molins, J. Llorca, *Catal. Today* **138**, 193 (2008)
- M. Ramamoorthy, A.A. Pisal, R.S. Rengasamy, A.V. Rao, *J. Porous Mater.* (2017). <https://doi.org/10.1007/s10934-017-0431-0>
- J.E. Fesmire, J.P. Sass, *Cryogenics* **48**, 223 (2008)
- K.I. Jensen, J.M. Schultz, F.H. Kristiansen, *J. Non-Cryst. Solids* **350**, 351 (2004)
- L.W. Hrubesh, R.W. Pekala, *J. Mater. Res.* **9**, 731 (1994)
- M. Moragues, *Aerogel-based Composite/Hybrid Nanomaterials for Cost-Effective Building Super-Insulation Systems*, Printed Pamphlet (2011)
- D.B. Mahadik, A.V. Rao, R. Kumar, S.V. Ingale, P.B. Wagh, S.C. Gupta, *J. Porous Mater.* **19**, 87 (2012)
- J.L. Gurav, A.V. Rao, D.Y. Nadargi, H. Park, *J. Mater. Sci.* **45**, 503 (2010)
- M. de Fátima Júlio, L.M. Ilharco, *Microporous Mesoporous Mater.* **199**, 29 (2014)
- X. Yang, Y. Sun, D. Shi, J. Liu, *Mater. Sci. Eng. A* **528**, 4830 (2011)
- X. Yang, Y. Sun, D. Shi, *J. Non-Cryst. Solids* **358**, 519 (2012)
- B. Yuan, S. Ding, D. Wang, G. Wang, H. Li, *Mater. Lett.* **75**, 204 (2012)
- Z. Li, L. Gong, X. Cheng, S. He, C. Li, H. Zhang, *Mater. Des.* **99**, 349 (2016)
- A. Ślosarczyk, M. Barekowski, S. Niemier, P. Jakubowska, *J. Sol Gel Sci. Technol.* **76**, 227 (2015)
- A. Ślosarczyk, S. Wojciech, Z. Piotr, J. Paulina, *J. Non-Cryst. Solids* **416**, 1 (2015)
- M.M. Koebel, L. Huber, S. Zhao, W.J. Malfait, *J. Sol Gel Sci. Technol.* **79**, 308 (2016)
- J.D. Feng, D. Le, S.T. Nguyen, V.T.C. Nien, D. Jewell, H.M. Duong, *Colloid Surf. A* **506**, 298 (2016)
- E.P. Barrett, L.G. Joyner, P.P. Halenda, *J. Am. Chem. Soc.* **73**, 373 (1951)
- J. Villarroel-Rocha, D. Barrera, K. Sapag, *Microporous Mesoporous Mater.* **200**, 68 (2014)
- A.C. Pierre, E. Elaloui, G.M. Pajonk, *Langmuir* **14**, 66 (1998)
- S.D. Bhagat, Y.H. Kim, K.H. Suh, Y.S. Ahn, J.G. Yeo, J.H. Han, *Microporous Mesoporous Mater.* **112**, 504 (2008)
- P.B. Wagh, S.V. Ingale, *Ceram. Int.* **28**, 43 (2002)
- S.V. Ingale, P.B. Wagh, A.K. Tripathi, V.S. Kamble, R. Kumar, S.C. Gupta, *J. Porous Mater.* **18**, 567 (2011)
- X. Lu, M.C. Arduini-Schuster, J. Kuhn, O. Nilsson, J. Fricke, R.W. Pekala, *Science* **255**, 971 (1992)